PNAS RESEARCH ARTICLE | EARTH, ATMOSPHERIC, AND PLANETARY SCIENCES

East Asian summer monsoon delivers large abundances of very short-lived organic chlorine substances to the lower stratosphere

Laura L. Pan[a,1], Elliot L. Atlas[b,1], Shawn B. Honomichl[a], Warren P. Smith[a], Douglas E. Kinnison[a], Susan Solomon[c], Michelle L. Santee[d], Alfonso Saiz-Lopez[e], Johannes C. Laube[f], Bin Wang[g], Rei Ueyama[h], James F. Bresch[i], Rebecca S. Hornbrook[a], Eric C. Apel[a], Alan J. Hills[a], Victoria Treadaway[b,j,k], Katie Smith[b], Sue Schauffler[a,b], Stephen Donnelly[b,l], Roger Hendershot[a,b], Richard Lueb[a,b], Teresa Campos[a], Silvia Viciani[m], Francesco D'Amato[m], Giovanni Bianchini[m], Marco Barucci[m], James R. Podolske[h], Laura T. Iraci[h], Colin Gurganus[j,k], Paul Bui[h,n], Jonathan M. Dean-Day[h,n], Luis Millán[d], Ju-Mee Ryoo[h,o], Barbara Barletta[p], Ja-Ho Koo[q], Joowan Kim[r], Qing Liang[s], William J. Randel[a], Troy Thornberry[k], and Paul A. Newman[s]

Edited by Mark Thiemens, University of California San Diego, La Jolla, CA; received October 26, 2023; accepted February 12, 2024

Deep convection in the Asian summer monsoon is a significant transport process for lifting pollutants from the planetary boundary layer to the tropopause level. This process enables efficient injection into the stratosphere of reactive species such as chlorinated very short-lived substances (Cl-VSLSs) that deplete ozone. Past studies of convective transport associated with the Asian summer monsoon have focused mostly on the south Asian summer monsoon. Airborne observations reported in this work identify the East Asian summer monsoon convection as an effective transport pathway that carried record-breaking levels of ozone-depleting Cl-VSLSs (mean organic chlorine from these VSLSs ~500 ppt) to the base of the stratosphere. These unique observations show total organic chlorine from VSLSs in the lower stratosphere over the Asian monsoon tropopause to be more than twice that previously reported over the tropical tropopause. Considering the recently observed increase in Cl-VSLS emissions and the ongoing strengthening of the East Asian summer monsoon under global warming, our results highlight that a reevaluation of the contribution of Cl-VSLS injection via the Asian monsoon to the total stratospheric chlorine budget is warranted.

Asian summer monsoon | convective transport | very short-lived ozone-depleting substances | stratospheric ozone

Significance

Recent measurements onboard high-altitude research aircraft detected large abundances of very short-lived ozone-depleting substances (VSLSs) over the western Pacific in the outflow of East Asian summer monsoon convection. The measurements in the lower stratosphere above the East Asian monsoon are more than double the concentration of those previously reported from the same layer of the atmosphere in the tropics. These observations suggest that 1) the contribution of VSLSs to the stratospheric chlorine budget may be larger than currently estimated, and 2) when combined with intense emissions of VSLSs in east Asia, East Asian monsoon convection provides a significant yet overlooked pathway for these anthropogenic ozone-depleting substances to enter the stratosphere.

The Asian summer monsoon (ASM), a significant element of the climate system, has been studied as a regional weather pattern for centuries. Only in recent decades has its role in global constituent transport been recognized, largely owing to observations made from satellites (1). The ASM is of particular interest because its associated deep convective systems rapidly transport air masses from the planetary boundary layer (PBL) in one of the most polluted regions on the planet to the upper troposphere and lower stratosphere (UTLS). An annually recurring layer with a distinct chemical signature and aerosol composition forms at the tropopause level within the ASM UTLS anticyclone during boreal summer (2–5). Detailed information on the chemical and microphysical changes in the UTLS induced by this annually recurring transport process is necessary for the accurate representation of the role of the ASM in chemistry-climate models. Targeted measurements using high-altitude research aircraft, in addition to ground-based and balloon-borne observations, provide data essential for understanding physical processes and constraining chemistry-climate models. Two prior experiments provided valuable measurements of trace gases and aerosols in the region of the ASM anticyclone (6–8). The Asian summer monsoon Chemical and Climate Impact Project (ACCLIP), a field campaign conducted in summer 2022 using two high-altitude aircraft, the NSF National Center for Atmospheric Research (NCAR) Gulfstream V (GV) and the NASA WB-57, represents the latest large-scale effort of this kind. The ACCLIP campaign conducted a total of 29 research flights over the northwestern Pacific from July 31 to September 1, 2022, from an airbase in the Republic of Korea (see *SI Appendix*, Fig. S1 for flight tracks). The flights sampled air masses lofted by convection both inside and near the eastern edge of the ASM anticyclone. The observations include a large suite of trace gases and aerosols, mostly at altitudes between 12 and 19 km above sea level (asl), a layer not accessible by commercial aircraft. The data represent the largest set of in situ atmospheric composition measurements in the ASM region (see *SI Appendix* for further details).

The ASM system has two distinct components, the South Asian summer monsoon (SASM) and the East Asian summer monsoon (EASM). These components are controlled by different heat sources and respond differently to global warming. The circulation of

The authors declare no competing interest.

This article is a PNAS Direct Submission.

[1]To whom correspondence may be addressed. Email: liwen@ucar.edu or eatlas@rsmas.miami.edu.

This article contains supporting information online at https://www.pnas.org/lookup/suppl/doi:10.1073/pnas.2318716121/-/DCSupplemental.

Published March 14, 2024.

the EASM is projected to strengthen while that of the SASM is projected to weaken, although both systems are projected to have increased precipitation due to increased moisture content (9). The schematic in Fig. 1*A* shows the key elements of the two subcomponents, highlighting two convergence zones: the Monsoon Trough and the East Asia Subtropical Front. Up to now, the SASM has been considered the dominant process for injecting PBL air masses into the ASM anticyclone at the tropopause level (6, 10–13). The Monsoon Trough was identified as the central region for convective lofting of PBL air masses (13). A key outcome of ACCLIP is the identification of the EASM convection as a more impactful transport pathway for UTLS chemical composition and stratospheric ozone chemistry than previously considered.

In this study, we report higher concentrations of PBL pollutants at the tropopause level than any previously measured in the UTLS and link these high values to convective lofting by deep convection in the EASM. Our measurements include large abundances of very short-lived chlorinated substances (Cl-VSLSs) from anthropogenic sources. Specifically, we report the measurements of five short-lived chlorine compounds: dichloromethane (CH_2Cl_2), chloroform ($CHCl_3$), 1,2-dichloroethane ($C_2H_4Cl_2$), tetrachloroethene (C_2Cl_4), and 1,2-dichloropropane ($C_3H_6Cl_2$). The first four of these species have been observed in the UTLS and are known to contribute to the stratospheric chlorine budget and ozone depletion (19). The fifth gas, 1,2-dichloropropane, is observed for the first time in the UTLS. The atmospheric concentrations of these species are generally of concern because of their increasing emissions in recent years (20–23). In reporting these observations, we bring further attention to the transport capacity of the EASM in a region of high emissions and the system's potential relevance to the recovery of the ozone layer in a changing climate.

Results

Active 2022 East Asian Summer Monsoon. The 2022 ASM season was highly anomalous, marked by the historic flooding in Pakistan and an unprecedented heatwave over the Yangtze River Valley (24). Drastic changes in the ASM precipitation pattern were linked to the "triple-dip" La Niña-induced atmospheric circulation changes: the westward extension of the Western Pacific Subtropical High in the lower-mid troposphere and the northeastward expansion of the intensified ASM anticyclone in the upper troposphere (24, 25). While the circulation change created the drought conditions dominating the Yangtze River Valley, northern China and the Korean peninsula experienced abundant rainfall (26). Fig. 1*B* shows the anomalies of EASM convection in August 2022 scaled by the interannual variability using the monthly SD (σ). Here, the distribution of the deep convection anomaly is derived from satellite infrared (IR) brightness temperature (17) and is generally consistent with the observed precipitation anomaly (24, 26). The 2 to 3 σ positive anomalies highlight the active EASM convection in late summer along the East Asia Subtropical Front, which migrated northward from the location of the typical Meiyu front (16). Also shown in the figure is the shape and location of the anticyclone in August 2022 together with the 44-y climatology. Compared to the climatology, the 2022 anticyclone was enlarged and much more elongated, with its center shifted further east, such that it encompassed more of the East Asian convergence zone than in a typical season. The anomalies highlighted in Fig. 1*B* are the key elements of the circulation pattern change that contributed to the findings of the ACCLIP campaign.

To demonstrate the large-scale impact of the circulation pattern change and the active EASM convection on UT composition, we show, in Fig. 2, the 150 hPa distribution of carbon monoxide (CO) from the Microwave Limb Sounder (MLS) on the NASA Aura satellite (27). Chemically, UT CO is an ozone precursor and a major chemical sink of OH (28). The concentration of CO in this layer has a direct impact on the atmospheric oxidation capacity. In this work, we use CO mostly as a transport tracer to characterize the convection. CO is an effective tracer of convective transport of polluted PBL air because it has a relatively short chemical lifetime (1 to 2 mo) and strong emission sources from both human activities and biomass burning (13, 29). Because of common source regions and photochemistry in the PBL, a wide range of reactive species are expected to be elevated in the high-CO air mass (30, 31). Also shown in Fig. 2 are selected contours of the 150 hPa stream function, which characterizes the UT flow pattern. Two stream function contours are selected to mark the outer edge and the center of the ASM anticyclone. They are selected empirically based on the horizontal gradient of the stream function field, with the edge contour (4×10^6 m^2/s) identifying the region of maximum gradient and the center contour (25×10^6 m^2/s) surrounding the region of minimum gradient. The average August 2022 CO distribution and the location of the ASM anticyclone contrast strongly with the 17-y (2005–2021) average. The anomalous distribution shown here provides the large-scale chemical signature of the convective transport and the background for the airborne campaign.

EASM Convection as an Efficient Transport Pathway for PBL Pollutants to Reach the UTLS. ACCLIP airborne observations sampled ASM-lofted air masses mostly downwind of the monsoon convection. The regions of convective transport that contributed to air masses sampled by the flights, based on Lagrangian back trajectory model calculations (*Materials and Methods*), are shown in Fig. 3*A*. The distribution shows that both EASM and SASM convection contributed to the airborne samples, but the EASM region shows a higher frequency of convective influence, as a result of both active seasonal convection and the proximity of the flights to the East Asia Subtropical Front. In Fig. 3*B*, in situ measurements of CO are used to characterize the level of pollution in the convection-influenced air masses from different regions. In general, the air masses influenced by EASM convection are associated with higher measured CO mixing ratios. To contrast the regional pollutants from the EASM and SASM, we calculated domain-average CO mixing ratios from the in situ CO measurements grouped into each domain using back trajectories (black boxes in Fig. 3*B*). The average CO mixing ratio identified with the EASM domain (130 ppbv) is about 35% higher than that identified with the SASM (95 ppbv).

The much higher CO mixing ratios at the top of the EASM convection indicate that the EASM convergence zone is aligned with a far more polluted PBL. This is further demonstrated in Fig. 4, where vertical distributions of CO and CH_2Cl_2 are shown. The maximum 1-min average CO mixing ratio shown in Fig. 4*A*, ~ 320 ppbv near 15 km asl, is more than double the previous maximum high-altitude CO measured during the StratoClim campaign in the SASM region (~150 ppbv). The mean CO mixing ratio at this level, ~125 ppbv, is about 25% higher than the mean previously measured at this level in the SASM region (~100 ppbv).

Record-breaking Observations of Very short-lived Chlorinated Ozone-depleting Substances. Among the large number of pollutants transported in the high-CO PBL air masses, we focus on a group of species known as very short-lived ozone-depleting substances. This is a subgroup of ozone-depleting substances with local lifetimes shorter than ~0.5 years (19, 37, 38). In particular,

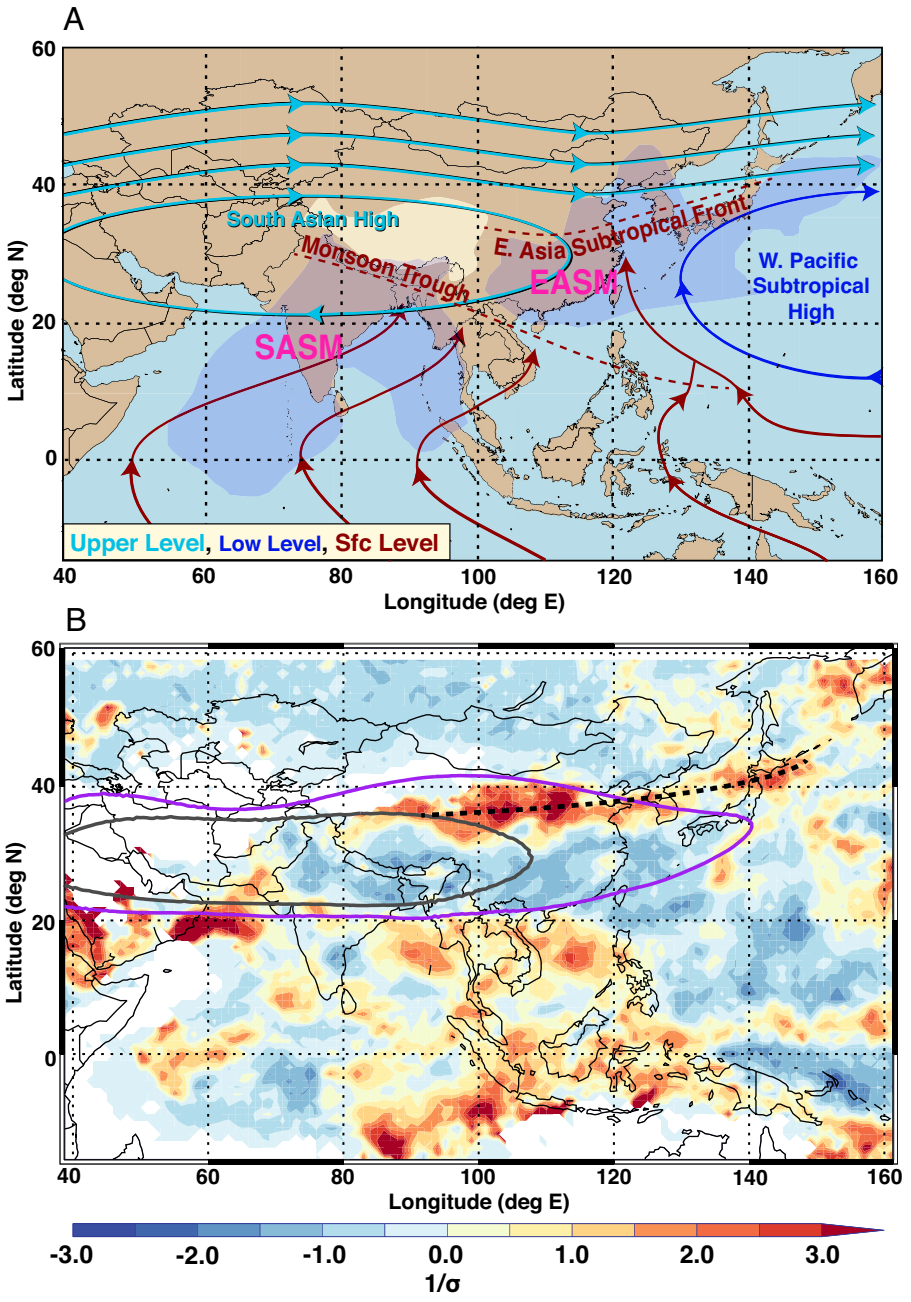

Fig. 1. ASM subcomponents and the active East Asian monsoon in August 2022. (*A*) Schematic of Asian summer monsoon subcomponents (14, 15). Flow patterns are shown at three levels represented by near surface (1,000 hPa "Sfc Level"), low level (850 hPa), and upper level (200 hPa). The East Asia Subtropical Front is the major rainfall-producing system; it is located on the northwest flank of the Western Pacific Subtropical High and migrates seasonally from around 25°N in May to 40°N in August. From mid-June to mid-July, the front is generally located from the Yangtze River basin to southern Japan, and the corresponding rainy season is called Meiyu in China or Baiu in Japan (16). (*B*) August 2022 anomalies of the occurrence frequency of convection defined by infrared brightness temperature $T_B < 235$ K using GPM MERGIR satellite data (17). The criterion identifies convective cloud tops above ~12 km altitude. Anomalies are calculated with respect to the climatological (2006–2022) August mean occurrence frequency at each location and scaled by the SD (σ). The position of the East Asia Subtropical Front for August 2022 is highlighted (black dashed curve). Also shown are 150 hPa geopotential height from the NCEP Climate Forecast System (CFS) data (18) 14,350-m contours for the 44-y (1979–2022) August climatology (gray) and August 2022 (purple)

we focus on the chlorinated VSLSs (Cl-VSLSs). Unlike long-lived ozone-depleting substances, VSLSs are not controlled under the Montreal Protocol. Nevertheless, these substances are under close watch and of increasing concern in recent years because many Cl-VSLSs originate primarily from anthropogenic sources, and their emissions have been rapidly increasing in recent decades. As a result, their contribution to stratospheric chlorine has increased by 61% between 2000 and 2017 (39). The increase is largely attributed to dichloromethane (CH_2Cl_2), the dominant component of Cl-VSLSs, comprising 70% of the Cl-VSLSs contribution to stratospheric chlorine (21, 37, 39). There are signs that the increasing VSLS levels may have impacts on the decrease of stratospheric chlorine. For example, between 2004 and 2017 the increase in Cl-VSLSs is estimated to have slowed the decline of upper stratospheric HCl (i.e., the major chlorine species in that region) by about 15% (39). Recent airborne observations have identified the impacts of ASM transport on the elevated Cl-VSLS levels in the UTLS (8, 40, 41).

Extremely high values of CH_2Cl_2 were observed near the tropopause in the region of East Asia during ACCLIP (Fig. 4*B*). Their

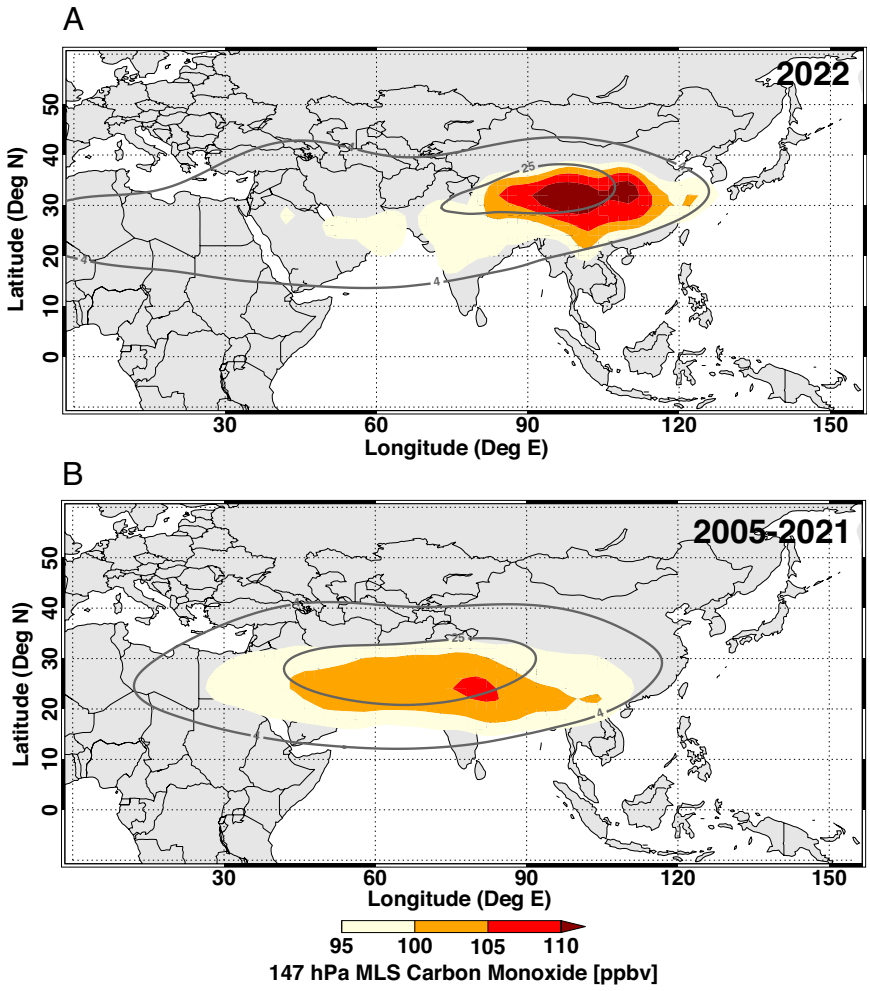

Fig. 2. Chemical signature of the strong EASM convective transport in 2022 from space. August average upper tropospheric carbon monoxide (CO) mixing ratios from satellite retrievals (MLS version 5 data at 147 hPa; see ref. 32 for details of MLS data quality and resolution) for (*A*) 2022 and (*B*) 2005–2021. Also shown are two selected contours of the 150 hPa stream function ([4, 25] × 10^6 m^2/s; based on the NCEP CFS data), which mark the outer edge and the center location of the ASM anticyclone.

vertical structure is similar to that of the CO distribution (Fig. 4*A*). Indeed, there is a strong positive correlation between CH_2Cl_2 and CO in the ACCLIP observations, as shown in Fig. 4*D*. The CH_2Cl_2 mixing ratios observed in the peak convective outflow layer near 15 km are as high as 600 pptv. This represents the highest value observed at the near-tropopause level; they are more than double those previously observed in the UT (8, 40). These strongly enhanced abundances arise from a combination of active deep EASM convection and the alignment of the convergence zone with intense Cl-VSLS emission sources. The occurrence in August 2022 of large anomalies in deep convection over the highly industrialized regions of Shandong and Hebei in the North China Plain, known to be among the largest CH_2Cl_2 emission sources in the world (22), is shown in Fig. 1*B*.

Injection of Cl-VSLSs to Layers above the Level of Zero Clear-sky Radiative Heating and the Tropopause. Theoretically, the level of zero clear-sky radiative heating (LZRH) marks the change from net radiative cooling below to net radiative heating above, which indicates the change of air mass large-scale vertical motion from subsidence to ascent (35). In Fig. 4 *A* and *B*, the layer between 360 K and 380 K potential temperature (θ) is shaded to highlight the measurements below the average tropopause, ~16.5 km or ~380 K, but above the estimated LZRH, ~360 K. The "C"-shape of the CO vertical distribution and the observed CO maximum of 320 ppbv near θ ~ 365 K show that the level of the main EASM convective outflow is above the LZRH. This leads to the important recognition that although the EASM convective transport did not reach the tropopause [defined by the temperature lapse rate, see WMO (42)], it lifted PBL pollutants to levels above the LZRH, where air masses undergo rising motion and are expected to enter the stratosphere.

Next, we quantify the concentration of total VSLS-sourced chlorine observed in the 1-km layer above the tropopause using tropopause-relative altitude coordinates (Fig. 4*C*). In this analysis, only WB-57 WAS data are used since the GV mostly sampled in the troposphere. Each sample's tropopause-relative coordinate is derived in reference to the nearest tropopause height determined from the WB-57 in situ sensor temperature data (*Materials and Methods*). The coordinate is then adjusted to the average tropopause height among all samples (36). The average in situ data-based tropopause altitude is 16.4 km and 378.3 K in θ. In Fig. 4*C*, the total chlorine includes the contributions from the five species listed in the Introduction: dichloromethane (CH_2Cl_2), chloroform ($CHCl_3$), 1,2-dichloroethane ($C_2H_4Cl_2$), 1,2-dichloropropane ($C_3H_6Cl_2$), and tetrachloroethene (C_2Cl_4). Among the 16 Cl-VSLSs observed during ACCLIP (*SI Appendix*, Table S1), these top five species have measured median concentrations above 1 pptv. The vertical distributions of these five Cl-VSLSs are shown in *SI Appendix*, Fig. S2.

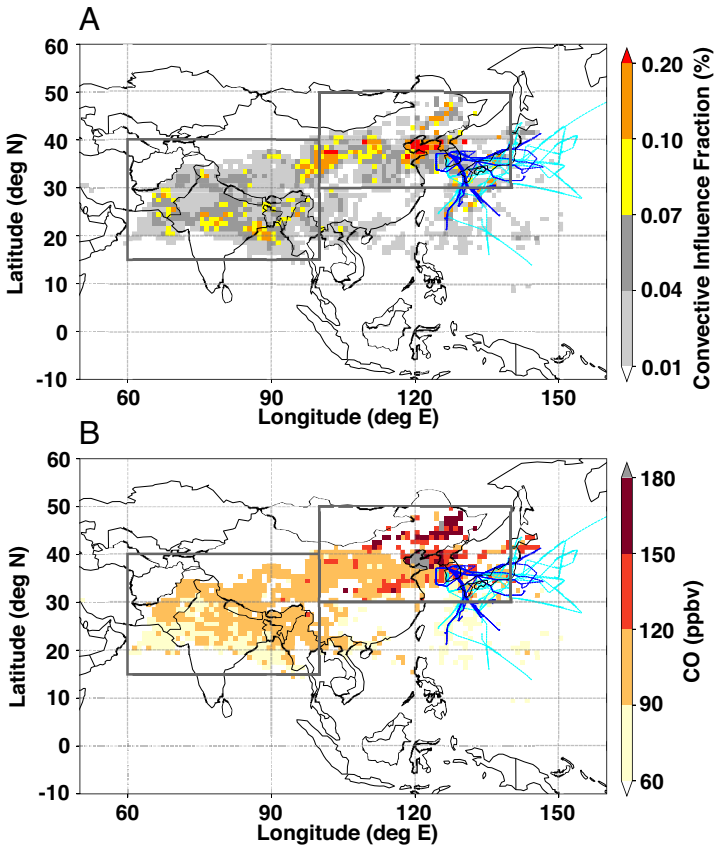

Fig. 3. Airborne observations of convective transport from SASM and EASM. (*A*) ACCLIP airborne campaign flight tracks (July 31 to September 1, 2022) and trajectory model derived convective influence (*Materials and Methods*). The distribution of convective influence for the airborne measurements at high altitudes (<200 hPa), estimated using trajectory calculations to connect the flight tracks with convection. Shaded pixels (1 × 1 degree) show the relative frequency of the colocation between convective clouds and back trajectories from the flight tracks (*Materials and Methods*). (*B*) The distribution of average CO mixing ratios for all airborne samples with convective influence within each pixel. The average CO for samples connected to the SASM and EASM domains (gray boxes) are approximately 95 and 130 ppbv, respectively. Note that the SASM average is consistent with the StratoClim measurements (33, 34). The blue and cyan lines show the flight tracks for the two research aircraft: the NASA WB-57 and the NSF/NCAR GV, respectively.

In general terms, both StratoClim and ACCLIP campaign data show that transport through the ASM is a significant pathway for stratospheric chlorine injection. However, the ACCLIP Cl-VSLS measurements highlight the importance of the EASM in that process. In Fig. 5, we provide relative-frequency distributions of total organic chlorine from Cl-VSLS source gases in the 1-km layer above the tropopause (LS) and the layer between the tropopause and the LZRH (UT), approximated by 360 to 380 K, together with the distributions of additional measurements from recent high-altitude aircraft campaigns, namely POSIDON data from 2016 (40) and StratoClim data from 2017 (8). Also given in the Fig. 5 insets are values of mean, median, range (defined as mean ± 1σ), and maximum for these datasets in both layers. The mean and range of ACCLIP observations in the LS layer are approximately a factor of 2 larger than those of the previous observations near the tropical tropopause reported in the WMO Ozone Assessment (19) (their Tables 1-5). They are ~50% larger than the StratoClim findings. In the UT layer, the ACCLIP mean chlorine value is about a factor of 4 larger than the tropical measurements and about a factor of 2 larger than the StratoClim data.

The Asian Monsoon Tropopause Structure and the Entry Point to the Stratosphere. Past model estimates of stratospheric chlorine entry values have typically used high-altitude aircraft measurements made at the tropical tropopause, i.e., at 16.5 to 17.5 km altitude and 20°S to 20°N latitude (39). The rationale is that tropospheric air primarily enters the stratosphere through the tropical tropopause. However, recent progress in the understanding of ASM UTLS dynamics and transport indicates that the ASM (rather than the tropical) tropopause is the dominant stratosphere entry point during boreal summer (1, 12, 13, 44, 45). Dynamically, the ASM region has the highest tropopause globally during the season (12, 46, 47). While the tropopause within the ASM anticyclone is higher than 380 K on average, the equatorial tropical tropopause is at or below 375 K. The monthly mean large-scale tropopause structure for the ACCLIP campaign season is shown in Fig. 6*A*.

On daily time scales, the anticyclonic flow at the tropopause level acts to produce large-scale stirring, enabling convectively lofted air at the near-tropopause level to mix with the surrounding lower stratospheric air via wave breaking, similar to the situation described by Holton et al. (48) for the extratropical lowermost stratosphere. This mixing process effectively transports chemical constituents in the monsoon upper troposphere into the surrounding lower stratosphere quasi-isentropically. A 40-y climatology constructed using trajectory calculations shows that UT air masses at the eastern edge of the ASM over the western Pacific enter the lower stratosphere within time scales of a week (49). To verify this behavior for August 2022, we have analyzed 20-d forward trajectories, with the vertical velocity based on diabatic heating, from WB-57 WAS samples collected in the UT layer between the LZRH and the local tropopause. The result (Fig. 6 *B* and *C*) shows that nearly 90% (~74%) of the sampled air masses enter the stratosphere within 20 (5) d. About 70% follow the anticyclonic flow to the tropical lower stratosphere and ~20% to the

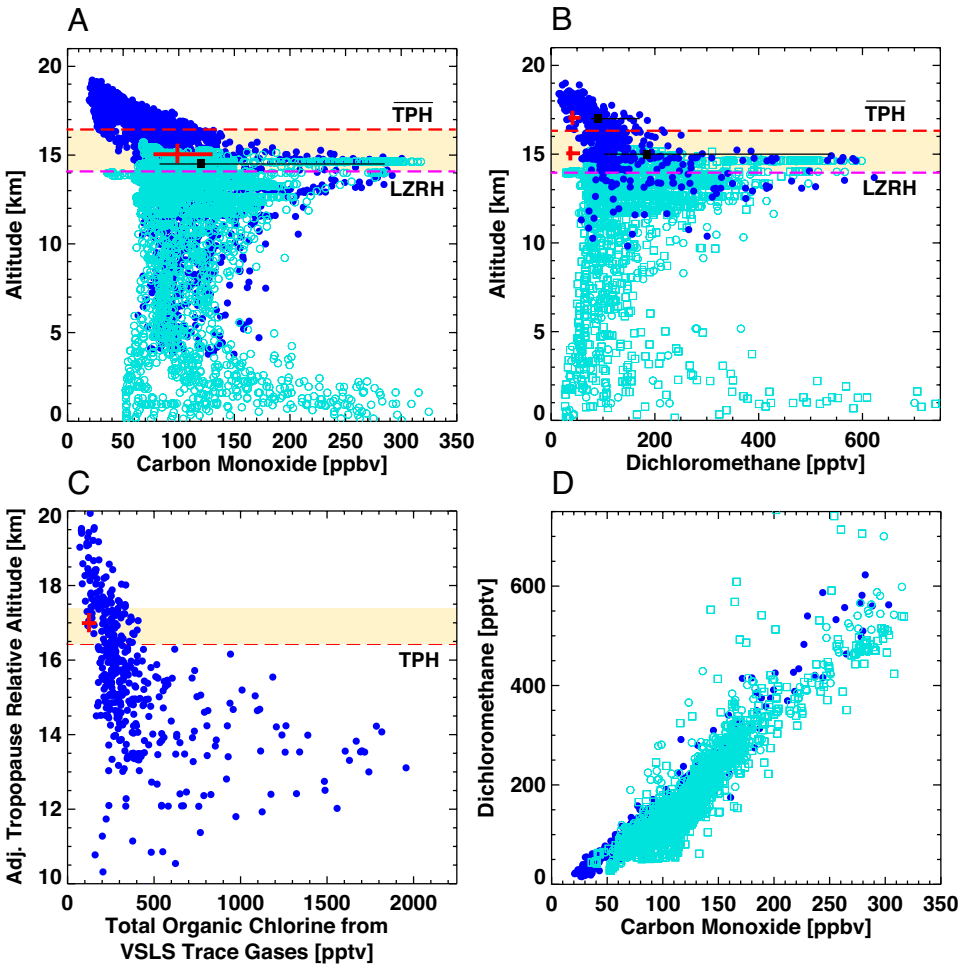

Fig. 4. Record-breaking CO and Cl-VSLS observed in the UTLS. (*A*) Vertical distribution of CO mixing ratios measured on the WB-57 (blue) and GV (cyan) aircraft (*Materials and Methods*) from all research flights (July 31 to September 1, 2022). The mean value and the 5th to 95th percentile for the 1-km layer near the level of zero clear-sky radiative heating (LZRH, magenta dashed line), approximated here by 360 K potential temperature (35), are marked by the filled black square and the thin black line, respectively. The average tropopause height is 16.5 km or ~380 K (red dashed line labeled TPH). The layer between the LZRH and the average tropopause is shaded in beige. The mean and range, represented by the 5th and 95th percentiles, for the StratoClim CO data (33) at the same levels are marked by the red vertical and horizontal lines, respectively. (*B*) Same as *A* but for dichloromethane (CH_2Cl_2) measured by WAS on WB-57 and TOGA and AWAS from the GV (*Materials and Methods*). For reference, the red symbols show the mean and range from previous measurements from the tropical tropopause region (see Tables 1-5 in ref. 19) and for the tropopause layer, 16.5 to 17.5 km. (*C*) Vertical distribution of total chlorine from WB-57 WAS measurements (*Materials and Methods*) of five primary Cl-VSLSs in tropopause-relative coordinates, adjusted by the mean tropopause height of 16.5 km (ref. 36 their equation 1). The red symbol marks the mean and range from previous measurements (see tables 1-5 in ref. 19). (*D*) A general positive correlation between CH_2Cl_2 and CO exemplifies the strong correlation between CO and many PBL pollutants measured during ACCLIP.

lowermost stratosphere in the Northern Hemisphere middle to high latitudes.

This convective transport behavior is well analyzed in a model study using synthetic regional tracers (44). Those authors estimated that nearly 20% of tropical lower stratospheric air is of Asian PBL origin during late boreal summer and fall. Therefore, to obtain an approximation of the impact of enhanced Cl-VSLSs measured during ACCLIP, we assume a 20% ASM contribution to the tropical lower stratosphere airmass and that the mean Cl-VSLS concentration in the layer above the LZRH is representative of a chemically aged Asian PBL. A mean of 500 pptv total VSLS-sourced organic chlorine during ACCLIP represents a 395 pptv greater source gas injection than the 105 pptv VSLS-sourced chlorine near the tropical tropopause reported in the 2022 WMO Ozone Assessment (19). This difference results in nearly 80 pptv more organic chlorine in the tropical lower stratosphere during summer and fall. Furthermore, a Lagrangian model study (45) estimates that the tropical lower stratosphere contains 5% of ASM air masses on an annual basis. Applied to the ACCLIP data, the 5% contribution of seasonal ASM transport would add 19 pptv to the organic chlorine in the tropical stratosphere annually, an 18% increase to the tropical lower stratosphere over that based solely on the tropical Cl-VSLS value (105 pptv) from the 2022 WMO Ozone Assessment (19). The key message is that the VSLS concentrations in the ASM UTLS should be used to constrain and verify model estimates of the amount of Cl-VSLSs injected into the stratosphere during the ASM season.

Discussion

Stratospheric ozone is a key component of the Earth's atmosphere and has direct links to the climate system. The success of the Montreal Protocol has led to the beginning of stratospheric ozone hole recovery (50). There is concern, however, that a rapid increase of anthropogenically sourced VSLSs, unregulated by the Montreal Protocol, could slow ozone recovery (38) and, together with naturally emitted halogenated VSLSs, induce stratospheric ozone loss that in turn has implications for future climate change (51, 52). The observations we report provide an important piece of information for quantifying the Cl-VSLS contribution to the stratospheric

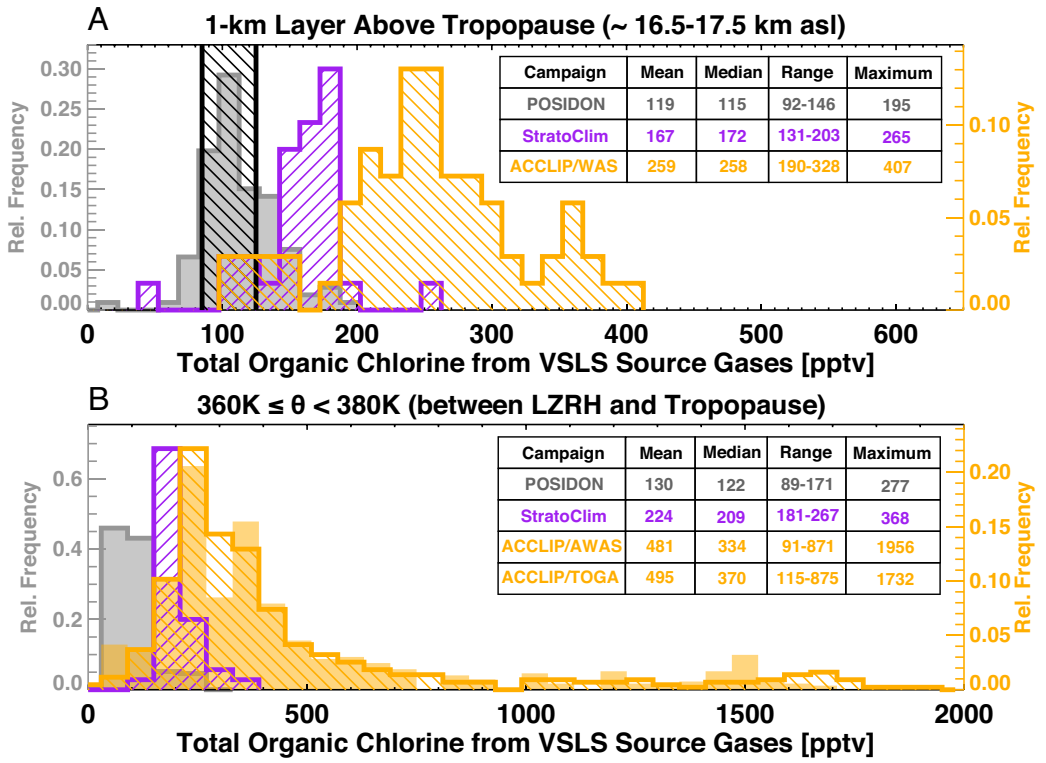

Fig. 5. Total VSLS-sourced organic chlorine. The relative frequency distributions of total organic chlorine from five Cl-VSLS source gases (dichloromethane, chloroform, 1,2-dichloroethane, 1,2-dichloropropane, and tetrachloroethene) from ACCLIP measurements (orange, right-hand *y* axis) in two layers: (*A*) within 1 km above the tropopause, representing the lower stratosphere (LS), and (*B*) 360 to 380 K potential temperature, representing the upper troposphere (UT) between the LZRH and the tropopause. The ACCLIP UT data in *B* were obtained by two instruments: TOGA-TOF (shaded) and AWAS/WAS (striped) (*Materials and Methods*). The LS data in *A* are from the WB-57 WAS measurements (*Materials and Methods*). Also shown for comparison in both (*A*) and (*B*) are WAS measurements over the tropical western Pacific during the October 2016 POSIDON campaign (gray; note that 1,2-dichloropropane was not included) and WAS measurements mostly sampling the SASM contribution during the summer 2017 StratoClim campaign (purple, sharing gray axis with POSIDON; note that 1,2-dichloropropane and tetrachloroethene were not included). The estimated contribution of Cl-VSLS source gases to the stratospheric chlorine budget in 2020 used in the 2022 WMO Ozone Assessment (105 ± 20 ppt) is shown in *A* (black). Mean, median, range (mean ± 1 σ), and maximum values of the total Cl-VSLSs for each dataset are given in the insets. Note that in (*A*) the POSIDON samples (106 cans) are selected within the 16.5 to 17.5 km layer, whereas the ACCLIP LS samples (69 cans) are selected within 1 km above the tropopause as determined using the nearest WB-57 in situ measurements. StratoClim samples (29 cans) are selected within 1 km above the tropopause using the ERA5 tropopause product (43).

chlorine budget. The ACCLIP campaign results identify the EASM to be a significant transport pathway relevant to stratospheric chemistry and the ozone layer, as it facilitates rapid injection of a large amount of PBL pollution into the stratosphere.

Globally, the largest emission sources of CH_2Cl_2 are known to be in South and East Asia (53). CH_2Cl_2 emissions are reported to have increased by 85% between 2006 and 2017, mostly due to increasing Asian emissions (21). It has also been hypothesized that the emissions from South Asia and East Asia have strong potential to be injected into the stratosphere, considering the depth of Asian monsoon convection (22, 39, 53, 54). While previous Asian monsoon observations have shown clear evidence of SASM contributions (8, 40), ACCLIP observations not only provide further evidence for this hypothesis but also highlight the key role of the EASM in injecting very short-lived ozone-depleting substances to the stratosphere.

The convection anomalies in 2022 reflect both temporal and spatial variations to the precipitation pattern, specifically the increased precipitation late in the ASM season and the anomalous northward migration of the convergence zone. In a typical year, active convection occurs earlier in the season, and the convergence zone (and thus strong deep convection) lies at lower latitudes (55). However, even then the climatological convergence zone still crosses intense Cl-VSLS sources along coastal east Asia, and emissions in those regions show signs of an increasing trend (22, 23). Therefore, although ACCLIP observations were made during an anomalous ASM season, large convective transport contributions from the EASM can be expected to occur even in less meteorologically extreme seasons.

The observations also underscore the need to examine the representation of deep convection and associated constituent transport in the current generation of global chemistry-climate models. Estimating VSLS source gas injection using models (39) requires evaluation and constraints. The ACCLIP campaign provided a unique set of dynamical and chemical observations for assessing the ability of models to accurately represent the injection of reactive chemical species into the stratosphere.

Adequate model representation of the EASM is also important for 21st-century chemistry-climate projections because the EASM is predicted to strengthen in a warming climate (56, 57). Globally, among the eight regional monsoons, the EASM is projected to have the highest sensitivity with respect to global warming (57). Stronger EASM convection will lead to higher Cl-VSLS contributions to stratospheric ozone-depleting substances, and subsequently ozone depletion, which need to be considered as a scenario in climate change predictions. The SASM is also situated above the largest Cl-VSLS source region and projected to have high sensitivity to the global warming trend (57). This work, therefore, provides evidence of monsoon–climate change linkages through enhanced Cl-VSLS injection and stratospheric ozone chemistry.

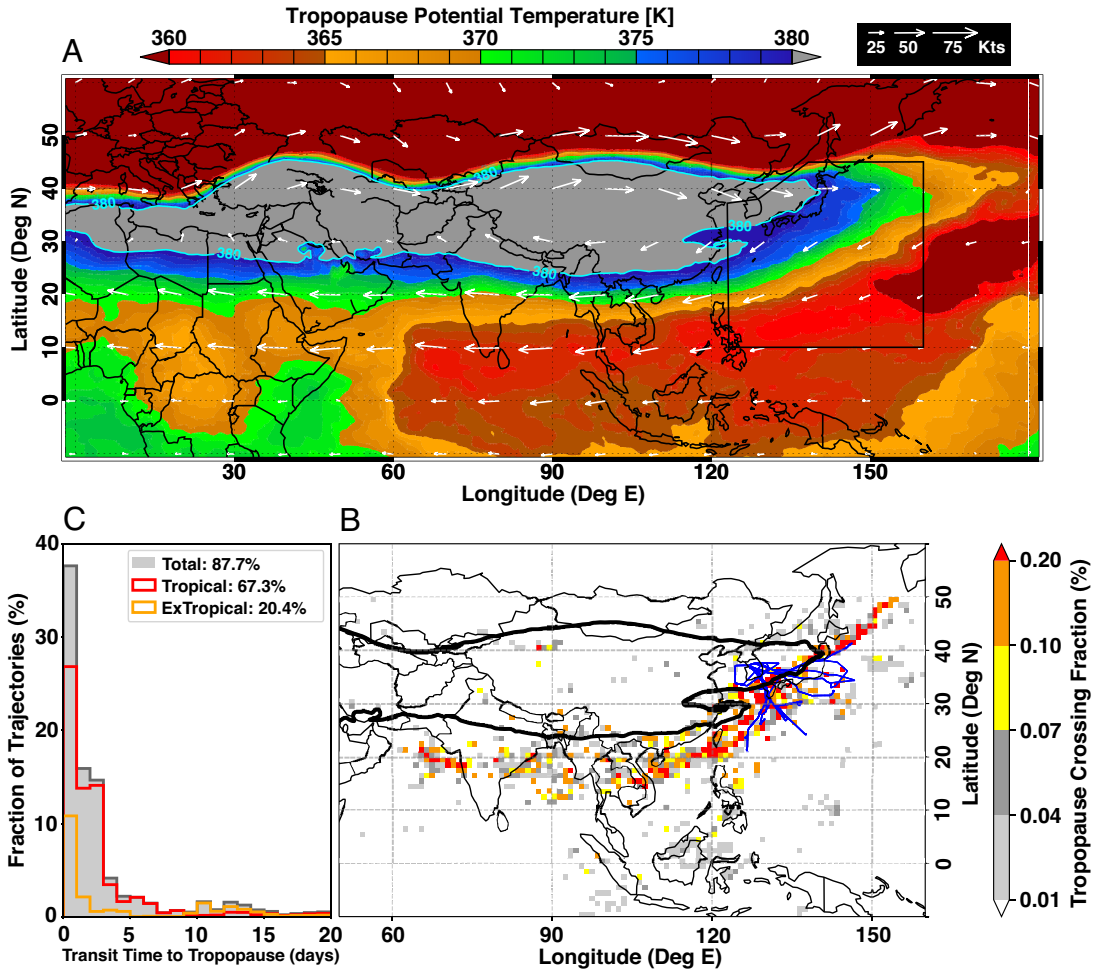

Fig. 6. August 2022 tropopause structure in potential temperature and the trajectory model diagnosis of the UT air mass entering the stratosphere. (*A*) The August 2022 monthly mean tropopause in potential temperature (color shaded contours) based on the ERA5 tropopause product (43). Also shown are the ERA5 horizontal winds at the 380 K level (white overlaid arrows). The rectangle (black) indicates the nominal ACCLIP flight region (Fig. 3). (*B*) The relative frequency map of the air mass tropopause crossing locations for all WB-57 WAS samples in the UT layer (between 360 K and the tropopause) (*Materials and Methods*). The WAS sampling locations are distributed along the WB-57 flight tracks (blue lines). To highlight the relationship between tropopause crossing frequency and the tropopause structure associated with the ASM anticyclone shown in panel *A*, the August 2022 monthly mean tropopause potential temperature at 380 K is shown (black contour). (*C*) Histogram of the fractions of trajectories crossing the tropopause within 20 d and their transit time distributions: the total fraction of sampled air masses that crossed the tropopause (gray), the fraction that followed the anticyclonic flow and entered the tropical lower stratosphere (red), and the fraction that entered the mid- to high-latitude lowermost stratosphere (orange). The tropical/extratropical separation is approximated by whether a trajectory's tropopause intercept was south or north (respectively) of the WAS measurement point at which a given trajectory was initialized.

Materials and Methods

In Situ Measurements of CO and Temperature. CO mixing ratios were measured on both the GV and the WB-57 aircraft. The WB-57 CO measurements are provided by three different sensors: COLD2 (Carbon Oxide Laser Detector 2; ref. 58), COMA (Carbon monOxide Measurement from Ames), and ACOS (NOAA Airborne Carbonic Oxides and Sulfide Spectrometer). The data from the three sensors are in good agreement and consistent in supporting the presented result. For the purposes of this study, the COLD2 CO data are displayed in Fig. 4.

The instrument COLD2, installed inside the right spearpod of the WB-57, is a midinfrared quantum cascade laser spectrometer based on the direct absorption technique in combination with a multipass cell. The instrument provides in situ CO mixing ratios with a time resolution of 1 s and an accuracy of 4%, without need of in-flight calibration. COLD2 in-flight sensitivity and precision are proved to be 1.5 ppb, increasing to about 900 ppt for 10-s integration time, and the 1-h long-term stability is ±2%. The CO values are inferred, during a postflight analysis, by the transmission spectra acquired during the flight.

The GV CO instrument operated by NCAR is an Aerodyne quantum cascade laser spectrometer (59) that utilizes direct absorbance of infrared radiation near 4.6 μm to quantify CO and nitrous oxide (N_2O). The instrument has an optical path length of 76 m, and the free space optics are continuously purged with dry nitrogen from which CO has been scrubbed to contain less than 1 ppbv. Hourly in-flight calibration checks confirmed the accuracy of flight data. The ACCLIP observations have a time resolution of 1 s, a precision of 0.3 ppbv, and an uncertainty of ±1 ppbv.

In situ static temperature data measured on the WB-57 are used in this work to calculate sampled tropopause height. The measurements are made by the NASA Ames Meteorological Measurement System (MMS), which provides calibrated static pressure, static temperature, and 3D winds at either 1 Hz or 20 Hz sampling rate. The 1-s time resolution data are used for this work. The temperature sensing element is NIST traceable, and inflight adiabatic compression compensation is determined from 3D wind calibration. Since 1984, the MMS has operated on several airborne platforms: the ER-2, Global-Hawk, DC-8, Sierra UAV, and AlphaJet. Based on the analyses of Scott et al. (60) and Gaines et al. (61), MMS static temperature has an accuracy of ±0.3 K at all altitudes, including the critically important UTLS region studied during ACCLIP.

Measurements of Chlorinated VSLSs by the TOGA-TOF, WAS, and AWAS. The NCAR Trace Organic Gas Analyzer with a TOFWERK high-resolution Time-of-Flight mass spectrometer (TOGA-TOF) was deployed on the NSF/NCAR GV during ACCLIP and provided measurements of Cl-VSLSs including CH_2Cl_2, $CHCl_3$, 1,2-dichloroethane, 1,2-dichloropropane, and C_2Cl_4. The TOGA-TOF is a fast online gas chromatograph/mass spectrometer (GC/MS) that sampled and processed in situ air for 35 s every 2 min during ACCLIP GV flights. Operational details of the TOGA system have been described previously (62). The TOGA-TOF was calibrated in flight during ACCLIP,

as well as in the laboratory prior to and following the deployment, using a series of ppb-level gas mixtures (Apel-Reimer Environmental, Inc.) diluted to typically observed mixing ratios using a clean-air generator.

Whole air samplers (WAS) were deployed on both the NSF/NCAR GV and the NASA WB-57 aircraft. The GV instrument (Advanced Whole Air Sampler, AWAS) collected samples into stainless steel canisters under computer control. Three sample modules contained 12 canisters each, and two sample modules contained 10 samples each. The latter sample modules had a different geometry but similar volume (1.3 L), and they were previously deployed in the NASA Global Hawk Aircraft (63). Samples were pressurized to 40 to 45 psia using two 2-stage metal bellows pumps. Sample collection times varied with altitude and module type, varying from about 4 to 60 s for the AWAS 12-can modules, with an average of about 26 s at the 12 to 15 km altitude range. The sample collection time for the 10-can modules was approximately 40 s and was nearly constant over the 12 to 15 km range. The WB-57 WAS instrument deployed 50 canisters per flight, as described in ref. (40). The sample collection time varied from about 14 s at 10 km to 120 s at 20 km, with an average of about 44 s between 14 km and 18 km (~360 to 400 K potential temperature). All sample canisters were precleaned in the field by repeated flushing/evacuation with wet nitrogen gas. After final evacuation, approximately 15-Torr water vapor was added to each canister to help passivate the canister interior surface. All samples from both aircraft were sent to the home laboratory at the completion of the field mission. Analyses took place from mid-October 2022 to mid-January 2023. Trace gas calibrations were based on in-house and commercial standards as described in refs. 64–66.

Trajectory Modeling and Satellite Data–based Convective Influence. To relate the ACCLIP observations to convective transport, a trajectory model is used to calculate 3D backward trajectories of idealized air parcels from the measurement locations and times. In the analysis shown in Fig. 3, "Convective influence" is identified when the air parcel's back trajectory is colocated with convection. Specifically, back trajectories are initialized in 1-min time intervals along the GV and WB-57 flight tracks and calculated with the TRAJ3D model (67) using three-dimensional kinematic wind fields from ERA5 reanalysis (68). Each 1-min trajectory initialization features 75 individual trajectories to account for trajectory path uncertainty. These are initially arranged in a 5 × 5 × 3 grid centered on the aircraft location, with a total dimension of 0.1 degrees latitude × 0.1 degrees longitude × 0.2 hPa. To investigate the ASM air mass contribution to the UTLS layer, trajectories are only included for aircraft measurements taken at pressures less than 200 hPa. Convection is represented by a convective cloud top altitude product, which is produced at 3-h intervals with a resolution of 0.25° × 0.25°. The method of constructing the database is described in ref. 69. Each convective influence case is identified by the first (i.e., most recent) "encounter" of a trajectory with convection within the previous 20 d, as determined by having an altitude lower than the colocated convective cloud top altitude derived from satellite observations. This approach is analogous to that used in refs. 70 and 71 for airborne campaigns over the tropical western Pacific.

To diagnose the tropopause crossing of air masses sampled in the UT (Fig. 6 *B* and *C*), forward trajectories are calculated using the TRAJ3D model and the ERA5 radiative temperature tendencies for vertical motion. 3D forward trajectories of idealized air parcels from the measurement locations and times of all WB-57 WAS sampling points within the UT layer (between the 360-K isentrope and the tropopause) are calculated for 20 d. Similar to the convective influence analysis, here the tropopause crossing is identified by colocation of the air parcels' forward trajectories with the tropopause, which is based on the ERA5 tropopause data product (43).

Data, Materials, and Software Availability. NCAR GV CO and VSLSs data can be ordered from the NCAR EOL ACCLIP Long Term Archive: https://data.eol.ucar.edu/project/ACCLIP. Analyses in this work used TOGA merge, AWAS/WAS merges, and 60-s merge: for TOGA-TOF merge: https://doi.org/10.26023/9TJ3-DT16-VZ00; for AWAS merge: https://doi.org/10.26023/2M8D-9C0V-AV0J; and for 60-s merge: https://data.eol.ucar.edu/dataset/620.053. NASA WB-57 data are available from NASA ESPO archive: https://www-air.larc.nasa.gov/cgi-bin/ArcView/acclip?WB57=1. Climate Forecast System (reanalysis and V2) data are available at the National Centers for Environmental Information archive: https://www.ncei.noaa.gov/products/weather-climate-models/climate-forecast-system. The GPM MERGIR satellite data are available here: https://disc.gsfc.nasa.gov/datasets/GPM_MERGIR_1/summary?keywords=Merged%20IR. DOI: 10.5067/P4HZB9N27EKU. The convective cloud top data can be accessed here: https://bocachica.arc.nasa.gov/nasaarc_cldalt/. ERA5 Tropopause Data (43) are available here: https://datapub.fz-juelich.de/slcs/tropopause/index.html. ERA5 products can be accessed from the ECMWF Climate Data Store: https://cds.climate.copernicus.eu/cdsapp#!/search?text=ERA5&type=dataset.

ACKNOWLEDGMENTS. The ACCLIP campaign was supported by NSF, NASA, and NOAA. This material is based upon work supported by the NSF National Center for Atmospheric Research, which is a major facility sponsored by the U.S. NSF under Cooperative Agreement No. 1852977. The GV data used in this work were collected using NSF's Lower Atmosphere Observing Facilities, which are managed and operated by NSF NCAR's Earth Observing Laboratory. L.L.P., D.E.K., and W.P.S. acknowledge the support of NSF grant AGS-1853929 for deployment. The COLD2 deployment is funded by European Space Agency (ESA) contract QA4EO-ACCLIP. J.R.P. and L.T.I. were supported by the NASA Earth Science Research and Analysis Program. E.L.A. acknowledges the grant from NSF AGS #1853948 and NASA NNX17AE43G and 80NSSC22K1284. R.U. and P.A.N. acknowledge the support from the NASA Upper Atmosphere Composition Observations Program. Q.L. acknowledges the support from the NASA Modeling, Analysis, and Prediction Program. S. Solomon appreciates support by NSF 2128617. Work at the Jet Propulsion Laboratory, California Institute of Technology, was carried out under a contract with the NASA (80NM0018D0004). J.K. acknowledges the support from the National Institute of Environmental Research (NIER2021-01-02-038). We thank the GV and WB-57 pilots and ground crew as well as the Osan Air Base staff for their support of the flight operations.

Author affiliations: [a]Atmospheric Chemistry Observations and Modeling Laboratory, NSF National Center for Atmospheric Research, Boulder, CO 80301; [b]Rosenstiel School of Marine, Earth, and Atmospheric Science, Department of Atmospheric Sciences, University of Miami, Miami, FL 33149; [c]Department of Earth, Atmospheric, and Planetary Sciences, Massachusetts Institute of Technology, Cambridge, MA 02139; [d]Jet Propulsion Laboratory, California Institute of Technology, Pasadena, CA 91109; [e]Department of Atmospheric Chemistry and Climate, Institute of Physical Chemistry Blas Cabrera, The Spanish National Research Council (CSIC), Madrid 28006, Spain; [f]Institute for Energy and Climate Research (IEK-7), Forschungszentrum Jülich, Jülich 52425, Germany; [g]Department of Atmospheric Sciences and International Pacific Research Center, The University of Hawaii, Honolulu, HI 96822; [h]NASA Ames Research Center, Moffett Field, CA 94035; [i]Mesoscale and Microscale Meteorology Laboratory, NSF National Center for Atmospheric Research, Boulder, CO 80301; [j]Cooperative Institute for Research in Environmental Sciences, University of Colorado Boulder, Boulder, CO 80309; [k]National Oceanic and Atmospheric Administration Chemical Sciences Laboratory, Boulder, CO 80305; [l]Department of Chemistry, Fort Hays State University, Hays, KS 67601; [m]National Institute of Optics, National Research Council, Sesto Fiorentino 50019, Italy; [n]Bay Area Environmental Research Institute, Moffett Field, CA 94035; [o]Science and Technology Corporation, Moffett Field, CA 94035; [p]Department of Chemistry, University of California Irvine, Irvine, CA 92697; [q]Department of Atmospheric Sciences, Yonsei University, Seoul 03722, Republic of Korea; [r]Department of Atmospheric Science, Kongju National University, Gongju 32588, Republic of Korea; and [s]NASA Goddard Space Flight Center, Greenbelt, MD 20771

Author contributions: L.L.P., E.L.A., T.T., and P.A.N. designed research; L.L.P., E.L.A., S.B.H., W.P.S., D.E.K., M.L.S., R.U., J.F.B., R.S.H., E.C.A., A.J.H., V.T., K.S., S. Schauffler, S.D., R.H., R.L., T.C., S.V., F.D., G.B., M.B., J.R.P., L.T.I., C.G., P.B., J.M.D.-D., L.M., J.-M.R., B.B., J.-H.K., J.K., Q.L., W.J.R., T.T., and P.A.N. performed research; L.L.P., E.L.A., S.B.H., W.P.S., R.U., R.S.H., E.C.A., V.T., K.S., T.C., S.V., F.D., G.B., M.B., J.R.P., L.T.I., C.G., P.B., J.M.D.-D., L.M., and J.-M.R. analyzed data; and L.L.P., E.L.A., W.P.S., D.E.K., S. Solomon, M.L.S., A.S.-L., J.C.L., B.W., R.U., J.F.B., R.S.H., T.C., S.V., F.D., P.B., J.M.D.-D., J.-M.R., T.T., and P.A.N. wrote the paper.

1. W. J. Randel *et al.*, Asian monsoon transport of pollution to the stratosphere. *Science* **328**, 611–613 (2010), 10.1126/science.1182274.
2. M. Park, W. J. Randel, A. Gettelman, S. T. Massie, J. H., Jiang Transport above the Asian summer monsoon anticyclone inferred from Aura Microwave Limb Sounder tracers. *J. Geophys. Res.* **112**, D16309 (2007), 10.1029/2006JD008294.
3. J.-P. Vernier, L. W. Thomason, J. Kar, CALIPSO detection of an Asian Tropopause Aerosol Layer. *Geophys. Res. Lett.* **38**, L07804 (2011), 10.1029/2010GL046614.
4. M. L. Santee *et al.*, A comprehensive overview of the climatological composition of the Asian summer monsoon anticyclone based on 10 years of Aura Microwave Limb Sounder measurements. *J. Geophys. Res. Atmos.* **122**, 5491–5514 (2017), 10.1002/2016JD026408.
5. P. Yu *et al.*, Efficient transport of tropospheric aerosol into the stratosphere via the Asian summer monsoon anticyclone. *Proc. Natl. Acad. Sci. U.S.A.* **114**, 6972–6977 (2017), 10.1073/pnas.17011701.
6. J. Lelieveld *et al.*, The South Asian monsoon-pollution pump and purifier. *Science* **361**, 270–273 (2018), 10.1126/science.aar2501.

7. M. Höpfner *et al.*, Ammonium nitrate particles formed in upper troposphere from ground ammonia sources during Asian monsoons. *Nat. Geosci.* **12**, 608–612 (2019), 10.1038/s41561-019-0385-8.
8. K. E. Adcock *et al.*, Aircraft-based observations of ozone-depleting substances in the upper troposphere and lower stratosphere in and above the Asian summer monsoon. *J. Geophys. Res. Atmos.* **126**, e2020JD033137 (2021), 10.1029/2020JD033137.
9. T. Li *et al.*, Distinctive South and East Asian monsoon circulation responses to global warming. *Sci. Bull.* **67**, 762–770 (2022), 10.1016/j.scib.2021.12.001.
10. J. W. Bergman, F. Fierli, E. J. Jensen, S. Honomichl, L. L. Pan, Boundary layer sources for the Asian anticyclone: Regional contributions to a vertical conduit. *J. Geophys. Res. Atmos.* **118**, 2560–2575 (2013), 10.1002/jgrd.50142.
11. B. Vogel, G. Günther, R. Müller, J. U. Grooß, M. Riese, Impact of different Asian source regions on the composition of the Asian monsoon anticyclone and of the extratropical lowermost stratosphere. *Atmos. Chemi. Phys.* **15**, 13699–13716 (2015).
12. L. L. Pan *et al.*, Transport of chemical tracers from the boundary layer to stratosphere associated with the dynamics of the Asian Summer Monsoon. *J. Geophys. Res. Atmos.* **121**, 14159–14174 (2016), 10.1002/2016JD025616.
13. L. L. Pan *et al.*, A multimodel investigation of Asian summer monsoon UTLS transport over the Western Pacific. *J. Geophys. Res. Atmos.* **127**, e2022JD037511 (2022), 10.1029/2022JD037511.
14. S. Tao, L. Chen, "A review of recent research on the East Asian summer monsoon in China" in *Monsoon Meteorology*, C.-P. Chang, T. N. Krishnamurti, Eds. (Oxford University Press, 1987), pp. 60–92.
15. B. Wang, H. Lin, Rainy season of the Asian–Pacific Summer Monsoon. *J. Climate* **15**, 386–398 (2002).
16. Y. Ding, D. R. Sikka, "Synoptic systems and weather" in *The Asian Monsoon* (Springer Praxis Books. Springer, Berlin, Heidelberg, 2006). 10.1007/3-540-37722-0_4.
17. J. John, J. Bob, X. Pingping, NCEP/CPC L3 Half Hourly 4km Global (60S – 60N) Merged IR V1, Edited by Andrey Savtchenko, Greenbelt, MD, Goddard Earth Sciences Data and Information Services Center (GES DISC) (2017). https://doi.org/10.5067/P4HZB9N27EKU. Accessed 03 August 2022.
18. S. Saha *et al.*, The NCEP climate forecast system Version 2. *J. Clim.* **27**, 2185–2208 (2014), 10.1175/JCLI-D-12-00823.1.
19. J. C. Laube, S. Tegtmeier, "Update on ozone-depleting substances (ODSs) and other gases of interest to the montreal protocol" in *Scientific Assessment of Ozone Depletion* (World Meteorological Organization, Geneva, Switzerland, 2022), Chap. 1, vol. 278.
20. X. Fang *et al.*, Rapid increase in ozone-depleting chloroform emissions from China. *Nat. Geosci.* **12**, 89–93 (2019), 10.1038/s41561-018-0278-2.
21. T. Claxton *et al.*, A synthesis inversion to constrain global emissions of two very short lived chlorocarbons: Dichloromethane, and perchloroethylene. *J. Geophys. Res. Atmos.* **125**, e2019JD031818 (2020), 10.1029/2019JD031818.
22. M. An *et al.*, Rapid increase in dichloromethane emissions from China inferred through atmospheric observations. *Nat. Commun.* **12**, 7279 (2021), 10.1038/s41467-021-27592-y.
23. M. An *et al.*, 2023, anthropogenic chloroform emissions from china drive changes in global emissions. *Environ. Sci. Technol.* **57**, 13925–13936 (2023), https://pubs.acs.org/doi/abs/10.1021/acs.est.3c01898.
24. C. He *et al.*, Extremely hot East Asia and flooding western South Asia in the summer of 2022 tied to reversed flow over Tibetan Plateau. *Clim. Dyn.* **61**, 2103–2119 (2023), 10.1007/s00382-023-06669-y.
25. S. Tang *et al.*, Linkages of unprecedented 2022 Yangtze River Valley heatwaves to Pakistan flood and triple-dip La Niña. *NPJ Clim. Atmos. Sci.* **6**, 44 (2023), 10.1038/s41612-023-00386-3.
26. B. Wang, Q. He, Global monsoon summary [in "State of the Climate in 2022"]. *Bull. Amer. Meteor. Soc.* **104**, S224–S227 (2023), 10.1175/BAMS-D-23-0078.1.
27. J. W. Waters *et al.*, The Earth Observing System Microwave Limb Sounder (EOS MLS) on the Aura satellite. *IEEE Trans. Geosci. Remote Sens.* **44**, 1075–1092 (2006), 10.1109/TGRS.2006.873771.
28. P. J. Crutzen, J. Fishman, Average concentrations of OH in the troposphere, and the budgets of CH4, CO, H2 and CH3CCl3. *Geophys. Res. Lett.* **4**, 321–324 (1977), 10.1029/GL004i008p00321.
29. B. N. Duncan *et al.*, Global budget of CO, 1988–1997: Source estimates and validation with a global model. *J. Geophys. Res.* **112**, D22301 (2007), 10.1029/2007JD008459.
30. M. Park *et al.*, Hydrocarbons in the upper troposphere and lower stratosphere observed from ACE-FTS and comparisons with WACCM. *J. Geophys. Res. Atmos.* **118**, 1–17 (2013), 10.1029/2012JD018327.
31. C. Wang *et al.*, Estimating halocarbon emissions using measured ratio relative to tracers in China. *Atmos. Environ.* **89**, 816–826 (2014), 10.1016/j.atmosenv.2014.03.025.
32. N. J. Livesey *et al.*, Version 5.0x Level 2 and 3 data quality and description document (Tech. Rep. No. JPL D-105336 Rev. B). Jet Propulsion Laboratory (2022), http://mls.jpl.nasa.gov.
33. S. Bucci *et al.*, Deep-convective influence on the upper troposphere–lower stratosphere composition in the Asian monsoon anticyclone region: 2017 StratoClim campaign results. *Atmos. Chem. Phys.* **20**, 12193–12210 (2020), 10.5194/acp-20-12193-2020.
34. von Hobe *et al.*, Upward transport into and within the Asian monsoon anticyclone as inferred from StratoClim trace gas observations. *Atmos. Chem. Phys.* **21**, 1267–1285 (2021), 10.5194/acp-21-1267-2021.
35. S. Fueglistaler *et al.*, Tropical tropopause layer. *Rev. Geophys.* **47**, RG1004 (2009), 10.1029/2008RG000267.
36. L. L. Pan, L. A. Munchak, Relationship of cloud top to the tropopause and jet structure from CALIPSO data. *J. Geophys. Res.* **116**, D12201 (2011), 10.1029/2010JD015462.
37. A. Engel *et al.*, "Update on ozone-depleting substances (ODSs) and other gases of interest to the Montreal Protocol" in *Scientific Assessment of Ozone Depletion: 2018* (Global Ozone Research and Monitoring Project-Rep. No. 58) (World Meteorological Organization, Geneva, Switzerland, 2018).
38. M. P. Chipperfield *et al.*, Renewed and emerging concerns over the production and emission of ozone-depleting substances. *Nat. Rev. Earth Environ.* **1**, 251–263 (2020).
39. R. Hossaini *et al.*, Recent trends in stratospheric chlorine from very short-lived substances. *J. Geophys. Res. Atmos.* **124**, 2318–2335 (2019), 10.1029/2018JD029400.
40. V. Treadaway *et al.*, Long-range transport of Asian emissions to the West Pacific tropical tropopause layer. *J. Atmos. Chem.* **79**, 81–100 (2022), 10.1007/s10874-022-09430-7.
41. V. Lauther *et al.*, In situ observations of CH_2Cl_2 and $CHCl_3$ show efficient transport pathways for very short-lived species into the lower stratosphere via the Asian and the North American summer monsoon. *Atmos. Chem. Phys* **22**, 2049–2077 (2022), 10.5194/acp-22-2049-2022.
42. World Meteorological Organization (WMO), Meteorology-a three dimensional science: Second session for the commission for aerology. *WMO Bull.* **6**, 134–138 (1957).
43. L. Hoffmann, R. Spang, An assessment of tropopause characteristics of the ERA5 and ERA-Interim meteorological reanalyses. *Atmos. Chem. Phys.* **22**, 4019–4046 (2022), 10.5194/acp-22-4019-2022.
44. C. Orbe, D. W. Waugh, P. A. Newman, Air-mass origin in the tropical lower stratosphere: The influence of Asian boundary layer air. *Geophys. Res. Lett.* **42**, 2015GL063937 (2015), 10.1002/2015GL063937.
45. F. Ploeger, P. Konopka, K. Walker, M. Riese, Quantifying pollution transport from the Asian monsoon anticyclone into the lower stratosphere. *Atmos. Chem. Phys.* **17**, 7055–7066 (2017), 10.5194/acp-17-7055-2017.
46. A. Dethof, A. O'neill, J. M. Slingo, H. G. J. Smit, A mechanism for moistening the lower stratosphere involving the Asian summer monsoon. *Quart. J. R. Meteorol. Soc.* **125**, 1079–1106 (1999). 10.1002/qj.1999.49712555602.
47. L. A. Munchak, L. L. Pan, Separation of the lapse rate and the coldpoint tropopauses in the tropics and the resulting impact on cloud top–tropopause relationships. *J. Geophys. Res. Atmos.* **119**, 7963–7978 (2014), 10.1002/2013JD021189.
48. J. R. Holton *et al.*, Stratosphere-troposphere exchange. *Rev. Geophys.* **33**, 403–439 (1995), 10.1029/95RG02097.
49. S. B. Honomichl, L. L. Pan, Transport from the Asian summer monsoon anticyclone over the western Pacific. *J. Geophys. Res. Atmos.* **125**, e2019JD032094 (2020), 10.1029/2019JD032094.
50. S. Solomon *et al.*, Emergence of healing in the Antarctic ozone layer. *Science* **353**, 269–274 (2016), 10.1126/science.aae0061.
51. J. Villamayor *et al.*, Very short-lived halogens amplify ozone depletion trends in the tropical lower stratosphere. *Nat. Clim. Chang.* **13**, 554–560 (2023), 10.1038/s41558-023-01671-y.
52. S. W. Son, Stratospheric ozone loss by very short-lived substances. *Nat. Clim. Chang.* **13**, 509–510 (2023), 10.1038/s41558-023-01687-4.
53. T. Claxton, R. Hossaini, O. Wild, M. P. Chipperfield, C. Wilson, On the regional and seasonal ozone depletion potential of chlorinated very short-lived substances. *Geophys. Res. Lett.* **46**, 5489–5498 (2019), 10.1029/2018GL081455.
54. J. R. Brioude *et al.*, Variations in ozone depletion potentials of very short-lived substances with season and emission region. *Geophys. Res. Lett.* **37**, L19804 (2010), 10.1029/2010GL044856.
55. Y. Ding, P. Liang, Y. Liu, Y. Zhang, Multiscale variability of Meiyu and its prediction: A new review. *J. Geophys. Res. Atmos.* **125**, e2019JD031496 (2020), 10.1029/2019JD031496.
56. C. He, Z. Wang, T. Zhou, T. Li, Enhanced latent heating over the Tibetan Plateau as a key to the enhanced East Asian summer monsoon circulation under a warming climate. *J. Clim.* **32**, 3373–3388 (2019), 10.1175/JCLI-D-18-0427.1.
57. C. Jin, B. Wang, J. Liu, Future changes and controlling factors of the eight regional monsoons projected by CMIP6 Models. *J. Clim.* **33**, 9307–9326 (2020), 10.1175/JCLI-D-20-0236.1.
58. S. Viciani, A. Montori, A. Chiarugi, F. D'Amato, A portable quantum cascade laser spectrometer for atmospheric measurements of carbon monoxide. *Sensors* **18**, 2380 (2018), 10.3390/s18072380.
59. J. B. McManus *et al.*, Application of quantum cascade lasers to high-precision atmospheric trace gas measurements. *Opt. Eng.* **49**, 111124-1–111124-11 (2010), 10.1117/1.3498782.
60. S. G. Scott, T. P. Bui, K. R. Chan, S. W. Bowen, The meteorological measurement system on the NASA ER-2 aircraft. *J. Atmos. Oceanic Technol.* **7**, 525–540 (1990).
61. S. E. Gaines, S. W. Bowen, R. S. Hipskind, T. P. Bui, K. R. Chan, Comparisons of the NASA ER-2 meteorological measurement system with radar tracking and radiosonde data. *J. Atmos. Oceanic Technol.* **9**, 210–225 (1992).
62. E. C. Apel *et al.*, Upper tropospheric ozone production from lightning NOx-impacted convection: Smoke ingestion case study from the DC3 campaign. *J. Geophys. Res. Atmos.* **120**, 2505–2523 (2015), 10.1002/2014JD022121.
63. M. A. Navarro *et al.*, Airborne measurements of organic bromine compounds in the Pacific tropical tropopause layer. *Proc. Natl. Acad. Sci. U.S.A.* **112**, E7155–E7155 (2015).
64. S. M. Schauffler *et al.*, Distributions of brominated organic compounds in the troposphere and lower stratosphere. *J. Geophys. Res.* **D17**, 21513–21536 (1999).
65. F. Flocke *et al.*, An examination of chemistry and transport processes in the tropical lower stratosphere using observations of long-lived and short-lived compounds obtained during STRAT and POLARIS. *J. Geophys. Res* **104**, 26625–26642 (1999), 10.1029/1999JD900504.
66. S. J. Andrews *et al.*, A comparison of very short lived halocarbon (VSLS) and DMS aircraft measurements in the tropical west Pacific from CAST, ATTREX and CONTRAST. *Atmos. Measurem. Tech.* **9**, 5213–5225 (2016), 10.5194/amt-9-5213-2016.
67. K. P. Bowman, Large-scale isentropic mixing properties of the Antarctic polar vortex from analyzed winds. *J. Geophys. Res.* **98**, 23013–23027 (1993), 10.1029/93jd02599.
68. H. Hersbach *et al.*, The ERA5 global reanalysis. *Q. J. R. Meteorol. Soc.* **146**, 1999–2049 (2020), 10.1002/qj.3803.
69. L. Pfister, R. Ueyama, E. Jensen, M. Schoeberl, Deep convective cloud top altitudes at high temporal and spatial resolution. *Earth Space Sci.* **9**, e2022EA002475 (2022), 10.1029/2022EA002475.
70. R. Ueyama *et al.*, Dehydration in the tropical tropopause layer: A case study for model evaluation using aircraft observations. *J. Geophys. Res. Atmospheres* **119**, 5299–5316 (2014), 10.1002/2013JD021381.
71. W. P. Smith *et al.*, Diagnostics of convective transport over the Tropical Western Pacific from trajectory analyses. *J. Geophys. Res. Atmos.* **126**, e2020JD034341 (2021), 10.1029/2020JD034341.